



# Thin-layer formation of ellipsoidal gyrotactic swimmers in time-dependent hydrodynamic shear

Zexu Li<sup>1</sup> and Lei Fang<sup>1,2</sup> 

<sup>1</sup>Department of Civil and Environmental Engineering, University of Pittsburgh, Pittsburgh, PA 15261, USA

<sup>2</sup>Department of Mechanical Engineering and Materials Science, University of Pittsburgh, Pittsburgh, PA 15261, USA

**Corresponding author:** Lei Fang, [lei.fang@pitt.edu](mailto:lei.fang@pitt.edu)

(Received 4 December 2024; revised 11 June 2025; accepted 19 June 2025)

We investigated the dynamics of thin-layer formation by non-spherical motile phytoplankton in time-dependent shear flow, building on the seminal work of Durham *et al.* (2009 *Science* vol. 323, pp. 1067–1070), on spherical microswimmers in time-independent flows. By solving the torque balance equation for a microswimmer, we found that the system is highly damped for body sizes smaller than  $10^{-3}$  m, with initial rotational motion dissipating quickly. From this torque balance, we also derived the critical shear for ellipsoidal microswimmers, which we validated numerically. Simulations revealed that the peak density of microswimmers is slightly higher than the theoretical prediction due to the speed asymmetry of sinking and gyrotaxis above and below the predicted height. In addition, we observed that microswimmers with higher aspect ratios tend to form thicker layers due to slower angular velocity. Using linear stability analysis, we identified a thin-layer accumulation time scale, which contains two regimes. This theoretically predicted accumulation time scale was validated through simulations. In time-dependent flow with oscillating critical shear depth, we identified three accumulation regimes and a transitional regime based on the ratio of swimmer and flow time scales. Our results indicate that thin layers can form across time scale ratios spanning five orders of magnitude, which helps explain the widespread occurrence of thin phytoplankton layers in natural water bodies.

**Key words:** micro-organism dynamics

## 1. Introduction

For more than four decades, researchers have observed the presence of thin layers of phytoplankton, characterised by dense concentrations of phytoplankton confined within narrow horizontal bands. These layers are accumulations of plankton in a narrow depth layer but extending over kilometres (Dekshenieks *et al.* 2001; Moline *et al.* 2010), and the phytoplankton concentration can potentially be orders of magnitude higher than the background level (Ryan *et al.* 2008; Sullivan, Donaghay & Rines 2010), forming important ecological activity hotspots. Due to their ecological significance, several fluid mechanic mechanisms have been proposed for the thin-layer formation, including straining (Franks 1995; Osborn 1998), buoyancy (Alldredge *et al.* 2002), intrusion (Armi 1978; Phillips, Shyu & Salmun 1986; Kasai *et al.* 2010) and gyrotactic trapping (Durham, Kessler & Stocker 2009). Those proposed mechanisms have been discussed in the review by Durham & Stocker (2012).

The gyrotactic trapping mechanism is one of the most promising mechanisms for explaining motile, bottom-heavy phytoplankton accumulations, and it is consistent with field observations that the thin layer is frequently found at the depths where vertical shear, variation of horizontal velocity as a function of vertical distance, is enhanced (Dekshenieks *et al.* 2001; Seuront & Strutton 2003; Ryan *et al.* 2008; Sullivan *et al.* 2010). The balance of two types of torques leads to gyrotactic trapping. One is hydrodynamic torque, also called viscous torque. The hydrodynamic torque was originally derived in the seminal work by Jeffery (1922), where particles respond to local vorticity and rate of strain (applicable only to non-spherical particles). At the microswimmer length scale, the microswimmers experience a sea of gradients, and they experience linear hydrodynamic shear locally (Stocker 2012) because the body size of the microswimmers is much smaller than Kolmogorov length scales (Wheeler *et al.* 2019). Gravitational torques arise from the fact that a microswimmer's centre of mass is different from its geometric centre. Most gyrotactic phytoplankton are bottom heavy, i.e. the centre of mass is located lower than the geometric centre. Bottom-heavy phytoplankton generates a stabilising gravitational torque on the cell that acts to keep its swimming direction oriented opposite to gravity.

Much previous research has shown that the microswimmer/particle intrinsic mobility, hydrodynamic torque from local shear and gyrotaxis can independently or jointly generate preferential distribution in a wide range of flows. Kessler (1985) set up the torque balance of a spherical motile cell and theoretically and experimentally demonstrated the gyrotactic focusing of the motile cells in Poiseuille flow. In addition, Durham, Climent & Stocker (2011) demonstrate that the gyrotactic motility within a steady vortical flow can cause a tightly clustered aggregation of microorganisms. A similar effect has also been observed by Khurana, Blawdziewicz & Ouellette (2011) and Yazdi & Ardekani (2012) with only motility effects. It has been found that the hydrodynamic shear (Rusconi, Guasto & Stocker 2014) and flow velocity (Borgnino *et al.* 2019) can have non-trivial impacts on the orientation and spatial heterogeneity of swimmers resulting from their shapes and intrinsic mobility, in which the fluid shear can trap swimmers (Rusconi *et al.* 2014) and rod-like swimmers preferentially align with the flow velocity (Borgnino *et al.* 2019). Turbulence can also lead to the heterogeneous distribution of swimmers and particles (Squires & Eaton 1991; Monchaux, Bourgoin & Cartellier 2011; Ray & Collins 2011; Durham *et al.* 2013; Obligado *et al.* 2014; Pujara, Koehl & Variano 2018; Falkinhoff *et al.* 2020; Qiu, Marchioli & Zhao 2022). In isotropic turbulence, ellipsoidal swimmers preferentially sample regions of lower fluid vorticity and accumulate in those regions (Pujara *et al.* 2018). However, clustering and patchiness are much weaker in isotropic turbulence than in simple cellular or vortical flows (Torney & Neufeld 2007; Khurana *et al.* 2011) due to

the complex topology (Zhan *et al.* 2014). (Lovecchio *et al.* 2019) demonstrated that chain formation in motile phytoplankton significantly enhances their ability to migrate vertically in turbulent waters, especially under weak to moderate turbulence. (Gustavsson *et al.* 2016) and (Borgnino *et al.* 2018) complemented the analysis presented in (Lovecchio *et al.* 2019), particularly discussed the effect of shape in sampling up-welling/down-welling regions of turbulence and the role of swimming speed. Si & Fang have revealed the preferential accumulation of non-spherical motile swimmers' accumulation near Lagrangian coherent structures (Si & Fang 2021) and three regimes of preferential transport of such swimmers in strongly heterogeneous two-dimensional weakly turbulent flow with heterogeneous Reynolds number along one direction (Si & Fang 2022).

Hydrodynamic torque, gravitational torque as well as microswimmer's intrinsic motility can also combine to generate a clustering of thin layers at the surface of water bodies. In natural water bodies, the shear rate typically decreases with increasing depth. (Durham *et al.* 2009) showed that thin layers form at a depth where the shear rate exceeds a critical value  $S_C$ . Above the critical shear, hydrodynamic torque dominates, causing continuous cell rotation and resulting in a sinking motion due to settling velocity. Below the critical shear, gyrotactic forces stabilise the cell, allowing it to move upward while encountering higher shear. As a result, the swimmer tends to become trapped at the critical shear layer. At critical shear, the cell's upward speed vanishes, leading to an accumulation of cells. The critical shear is derived based on torque balance and is equal to the inverse of the gyrotactic time scale ( $\tau$ ), which  $\tau$  is known for a variety of species and is generally within 1–100 s (Kessler 1985; Hill & Häder 1997; Drescher *et al.* 2009; Durham *et al.* 2009). (Santamaria *et al.* 2014) investigated spherical gyrotactic trapping in Kolmogorov flows and discussed the effects of turbulence fluctuation on thin-layer formation. Bearon & Durham (2023) explored elongated gyrotactic trapping in Kolmogorov flow. (Berman *et al.* 2022) assessed the effect of elongation in steady Kolmogorov, while (Borgnino *et al.* 2022) investigated that effect both in steady and unsteady Kolmogorov flows.

Despite valuable insights from gyrotactic swimmers in Kolmogorov flow, significant opportunities remain in understanding the gyrotactic trapping mechanisms driving thin-layer generation in the depth-independent shear environments typical of oceans and lakes. A few key questions remain unanswered. First, how does the swimmer shape affect the formation of the thin layer? Second, how quickly does this thin layer emerge, i.e. what is the time scale of thin-layer accumulation? Third, how will the time-dependent flow modulate the thin layer? In this paper, we aim to address these knowledge gaps.

We start in § 2 by introducing the equations for torque balance, reviewing the equations for particle rotational motion and their simplification, and verifying our model. In § 3, we study the impact of a swimmer's non-spherical shape on thin-layer formation, deriving the thin-layer accumulation time scale, and reveal three distinct mechanisms for thin-layer accumulation when the background flow is time-dependent. We conclude our work in § 4.

## 2. Methods

### 2.1. Torque balance and agent-based model

We simulate particles as spheroids of which the sizes are described by  $d_s$ , the diameter of the equivalent sphere with the same volume as the spheroid. The shapes are described by  $\lambda$ , the aspect ratio given by  $a/b$ , where  $a$  is the length along the particle's axis of symmetry and  $b$  is the length of one of the orthogonal axes (figure 1). Here,  $L$  is the distance between the centroid and the centre of mass, while  $T_g = mgL \sin \phi$  is the gravitational torque due to the bottom-heavy characteristic, where  $m$  is the mass of the microswimmer,  $g$  is the

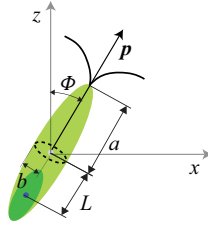


Figure 1. Sketch of ellipsoidal microswimmer. Only prolate spheroidal particles are considered, as no gyrotactic microswimmers are oblate. Here,  $a$  represents the length of the long semi-axis while  $b = c$  are the lengths of the short semi-axes for axisymmetric ellipsoids. The hydrodynamic shear lies in the  $x$ - $z$  plane (the  $y$ -axis points into the page), and only  $\partial u_x / \partial z$  is non-zero. The angle between vertical direction ( $z$ -axis) and swimming orientation ( $\mathbf{p}$ ) is the polar angle  $\phi$ . Here,  $L$  is the distance from the centroid to the centre of gravity. In the schematic, the flagella are shown only to indicate the direction of swimming.

acceleration due to gravity,  $\phi$  is the angle from the  $z$ -axis to the swimming direction  $\mathbf{p}$ , i.e. the polar angle. Conceptually, the polar angle  $\phi$  spans the range  $[-\pi, \pi]$ . However, as the primary focus of this paper is on the formation of thin layers, lateral displacement in the  $x$ -direction is not our main interest. Therefore, we restrict  $\phi$  to  $[0, \pi]$ , treating negative values of  $\phi$  as their positive counterparts by mirroring them across the  $z$ -axis. In this paper, we considered prolate ( $\lambda > 1$ ) spheroids since most gyrotactic microswimmers are prolate.

Starting from the equation of hydrodynamic torque  $\mathbf{T}$  for ellipsoids in general shear flow shown in Jeffery's seminal paper (Jeffery 1922)

$$\mathbf{T} = \begin{pmatrix} T_x \\ T_y \\ T_z \end{pmatrix} = \frac{16\pi\mu a^3}{3} \begin{pmatrix} \frac{b^2 + c^2}{b^2\beta_0 + c^2\gamma_0} \left( \frac{b^2 - c^2}{b^2 + c^2} S_{zy} + (\Omega_{zy} - \omega_x) \right) \\ \frac{c^2 + a^2}{c^2\gamma_0 + a^2\alpha_0} \left( \frac{c^2 - a^2}{c^2 + a^2} S_{xz} + (\Omega_{xz} - \omega_y) \right) \\ \frac{a^2 + b^2}{a^2\alpha_0 + b^2\beta_0} \left( \frac{a^2 - b^2}{a^2 + b^2} S_{yx} + (\Omega_{yx} - \omega_z) \right) \end{pmatrix}, \quad (2.1)$$

where  $S_{ij} = (1/2) (\partial_j u_i + \partial_i u_j)$ ,  $\Omega_{ij} = (1/2) (\nabla \times \mathbf{u})$ ,  $\mathbf{u}$  is the velocity of the background flow,  $U_x$  is the horizontal component of the background velocity field and  $\omega_i$  is particle's angular velocity. The shape parameters  $\alpha_0$ ,  $\beta_0$  and  $\gamma_0$  are given by,

$$\alpha_0 = \int_0^\infty \frac{dh}{(a^2 + h)\Delta}, \quad \beta_0 = \int_0^\infty \frac{dh}{(b^2 + h)\Delta}, \quad \gamma_0 = \int_0^\infty \frac{dh}{(c^2 + h)\Delta}, \quad (2.2)$$

where  $\Delta = [(a^2 + h)(b^2 + h)(c^2 + h)]^{1/2}$ , and  $a$ ,  $b$  and  $c$  are the semi-axes lengths along three axes for triaxial ellipsoids. The formula for shape factor integrals are provided in table 1.

Assuming the shear flow is generated by the vertical gradients of velocity in the  $x$ - $z$  plane, the sum of hydrodynamic and gravitational torques on an ellipsoid can be written as

$$T_y = \frac{16\pi\mu a^3}{3} \left[ \frac{b^2 + a^2}{b^2\beta_0 + a^2\alpha_0} \left( \frac{b^2 - a^2}{b^2 + a^2} \frac{\partial u_x}{\partial z} + (\Omega_y - \omega_y) \right) \right] - mgL \sin \phi, \quad (2.3)$$

The first term on the right-hand side involves the contribution of hydrodynamic torque. Both rate of strain and vorticity contribute to the hydrodynamic torque for non-spherical particles, while only vorticity contributes to the hydrodynamic torque when a swimmer

|                      | $\lambda > 1$  | $\lambda = 1$       | $0 < \lambda < 1$   |
|----------------------|--|---------------------|---|
| $\alpha_0$           | $-\frac{2}{\lambda^2 - 1} - \frac{\lambda\kappa}{\sqrt{\lambda^2 - 1}^3}$                | $\frac{2}{3}\kappa$ | $-\frac{\lambda}{2\sqrt{1 - \lambda^2}^3}(\kappa - \pi + 2\lambda\sqrt{1 - \lambda^2})$ |
| $\beta_0 = \gamma_0$ | $\frac{\lambda^2}{\lambda^2 - 1} + \frac{\lambda\kappa}{2\sqrt{\lambda^2 - 1}^3}$        | $\frac{2}{3}\kappa$ | $\frac{1}{\sqrt{1 - \lambda^2}^3}(\lambda(\kappa - \pi) + 2\sqrt{1 - \lambda^2})$       |
| $\kappa$             | $\log\left(\frac{\lambda - \sqrt{\lambda^2 - 1}}{\lambda + \sqrt{\lambda^2 - 1}}\right)$ | 1                   | $2 \arctan\left(\frac{\lambda}{\sqrt{1 - \lambda^2}}\right)$                            |

Table 1. Solution of shape factor integrals for ellipsoids with  $b = c$  and  $a = b\lambda$ .

is spherical. The second term on the right-hand side is gravitational torque. By setting  $T_y = 0$ , and  $\omega_y = 0$ , the static torque balance yields a constant polar angle  $\phi$  for time-independent shear rate,

$$\sin \phi = \frac{16\pi\mu a^3}{3mgL} \left( \frac{b^2}{b^2\beta_0 + a^2\alpha_0} \right) \frac{\partial u_x}{\partial z} = \tau \frac{\partial u_x}{\partial z}, \quad (2.4)$$

where  $\tau$  is the gyrotactic reorientation time scale, referring to the characteristic time it takes for microswimmers to reorient themselves due to gravitational torque.

Substituting the volume calculation formula of spheroids,  $V = 4/3\pi a^2 b$ , into (2.4), a simplified expression of  $\tau$  can be obtained

$$\tau = \frac{4\nu}{BgL(\beta_0/\lambda^2 + \alpha_0)}, \quad (2.5)$$

where  $B$  is the buoyancy, which is the density ratio of particle to fluid. With the gyrotactic reorientation time scale ( $\tau$ ), the equation of torque can be simplified as

$$T_y = mgL\tau \left[ \frac{\partial u_x}{\partial z} - (1 + \lambda^2)\omega_y - \frac{\sin \phi}{\tau} \right]. \quad (2.6)$$

Then, the angular acceleration can be derived as

$$\dot{\omega}_y = \frac{T_y}{I_y} = -\frac{5gL\tau}{b^2}\omega_y + \frac{5gL\tau}{a^2 + b^2} \left[ \frac{\partial u_x}{\partial z} - \frac{\sin \phi}{\tau} \right], \quad (2.7)$$

where  $I_y$  is the moment of inertia of the ellipsoidal swimmers. The angular velocity can be solved as

$$\omega_y = -\frac{1}{\lambda^2 + 1} \left( \frac{\partial u_x}{\partial z} \Big|_{t=0} - \frac{\sin \phi_0}{\tau} \right) e^{-\frac{5gL\tau}{b^2}t} + \frac{1}{1 + \lambda^2} \left( \frac{\partial u_x}{\partial z} - \frac{\sin \phi}{\tau} \right), \quad (2.8)$$

where  $\phi_0$  is the initial polar angle. We arrive at the question of the motion of angular velocity of an ellipsoid particle experiencing both viscous and gravitational torques. Since we assume that flow has no velocity out of the  $x$ - $z$  plane, the angular velocity is a scalar. Moreover, the angular velocity consists of an exponentially decaying time-varying part and a steady part.

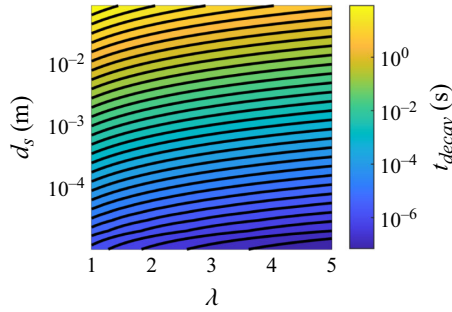


Figure 2. Colour map of the decaying time scale  $t_{decay}$  with equivalent diameter  $d_s$  and aspect ratio  $\lambda$ . The colour bar is presented on a logarithmic scale.

To determine how quickly the first term decays, we quantify the magnitude of its decaying time scale

$$t_{decay} = \frac{b^2}{5gL\tau} = \frac{Bb^2(\beta_0 + \lambda^2\alpha_0)}{20\nu\lambda^2}. \quad (2.9)$$

The decay time scale is a function of both the swimmer's size and shape. Figure 2 shows  $t_{decay}$  is smaller than  $10^{-2}$  s when  $d_s$  is smaller than  $10^{-3}$  m for  $\lambda$  between 1 and 5, meaning the system is highly damped and inertia can be ignored even for relatively large swimmers such as *Euglena gracilis*, *Ceratium* and species belong to Copepod. Most gyrotactic microswimmers are smaller than  $10^{-3}$  m and have an aspect ratio between 1 and 5. Based on that, we proposed an agent-based model for gyrotactic ellipsoidal swimmers

$$\omega_y = \frac{1}{1 + \lambda^2} \left( \frac{\partial u_x}{\partial z} - \frac{\sin \phi}{\tau} \right), \quad (2.10)$$

$$\mathbf{v} = \mathbf{u} + v_p \mathbf{p} + \mathbf{v}_{settle}, \quad (2.11)$$

$$\phi = \omega_y \Delta t + \Delta \phi, \quad (2.12)$$

where  $\mathbf{u}$  is the velocity of background flow while  $\mathbf{p}$  indicates the swimming direction.  $\mathbf{v}_{settle}$  is the settling velocity, which can be written as

$$\mathbf{v}_{settle} = -v_1 \mathbf{e}_z - (v_3 - v_1)(\mathbf{e}_z \cdot \mathbf{p})\mathbf{p}, \quad (2.13)$$

where  $v_1$  and  $v_3$  are the Stokesian terminal velocities of a spheroid in a quiescent fluid with its symmetry axis orientated orthogonal to and parallel to the gravity direction. To describe randomness existing in the swimming direction of a group of swimmers, we add noise at each time step, which is modelled as  $\Delta \phi = \pm(2D_R \Delta t)^{1/2}$  with rotational diffusivity  $D_R = 0.01 \text{ s}^{-1}$  (Durham *et al.* 2009).

## 2.2. Model verification

To verify our agent-based model of spheroidal microswimmers, we utilise the parameters of a typical gyrotactic microswimmer, *Chlamydomonas nivalis*, in our simulation, with  $v_p = 80 \mu\text{m s}^{-1}$ ,  $d_s = 10 \mu\text{m}$ ,  $B = 1.05$  and  $L = 0.06 \mu\text{m}$ . When setting  $\lambda = 1.001$ , we recover the experimental conditions of (Durham *et al.* 2009). The background flow is assumed to be a linear shear flow with kinematic viscosity  $\nu = 1 \times 10^{-6} \text{ m}^2 \text{ s}^{-1}$ . The shear rate can be expressed as  $\partial u / \partial z = 3z - 0.3$ , which varies linearly from  $-0.3$  to  $0.6 \text{ s}^{-1}$  when

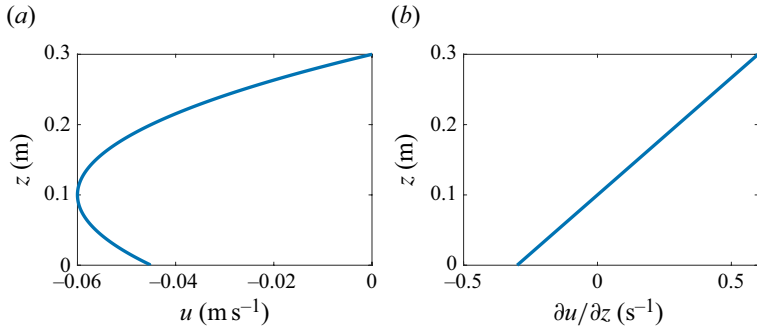


Figure 3. Flow conditions: (a) velocity profile and (b) shear profile of the background flow.

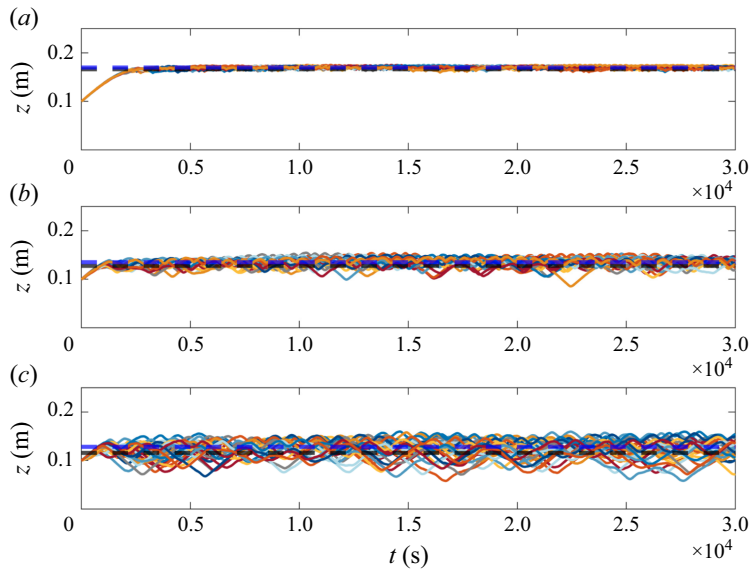


Figure 4. Time evolution of the heights of a group of microswimmers with (a)  $\lambda = 1.001$ , (b)  $\lambda = 2$  and (c)  $\lambda = 3$ . The black dashed line represents the theoretical prediction of the depth of critical shear ( $1/\tau$ ) according to (2.5), while the blue dashed line shows the average ensemble depth of the thin layer from the simulation.

$z$  changes from 0 to 0.3 m (figure 3). Initially, 500 spheroidal active particles are released at  $x = 0$  m and  $z = 0.1$  m with uniformly distributed random orientations. The time step is set to 0.01 s.

Figure 4 shows time variations in the depth of a group of gyrotactic microswimmers with different body shapes, and the dashed lines are the predicted accumulation depths. We observe that microswimmers accumulate near the predicted critical shear depths. In the beginning, the swimmers are located in a region with relatively low shear ( $z = 0.1$  m) with random orientation. The gravitational torque dominates the rotational motion, directing the microswimmers to go upward. However, when microswimmers go above the theoretically predicted depth, the hydrodynamic torque dominates and drives microswimmers to rotate continuously. When the swimmer rotates continuously, its intrinsic mobility lacks directional bias in the vertical direction, and the gravitational settling moves the microswimmers downward gradually. Finally, those swimmers will



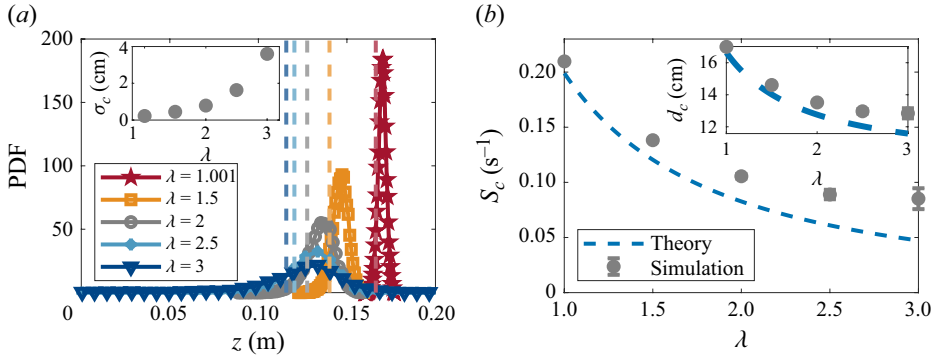


Figure 5. (a) The PDFs of the depths of microswimmers at steady states with a series of aspect ratios from 1.001 to 3. The vertical dashed lines indicate the theoretical predictions of the depth of critical shears ( $1/\tau$ ). The inset shows the standard deviations of the PDFs as a function of  $\lambda$ , where the standard deviations characterise the thickness of the thin layer. (b) Comparison of critical shear between numerical results and theoretical prediction. The inset figure shows numerical accumulation depth and corresponding theoretical predictions.

accumulate at a specific height, where local shear is equal to critical shear, and form a thin layer in the background flow. Due to the rotational diffusivity in the simulation, the microswimmers' orientations will be perturbed, and the aforementioned process will continue. When  $\lambda = 1.001$ , we observe a thin-layer accumulation where the local shear is approximately  $0.2 \text{ s}^{-1}$ , which is consistent with the (Durham *et al.* 2009) experiments with nearly spherical microswimmers (*Chlamydomonas nivalis*). The reproduction of the experimental observation shows that our simulation is reliable.

### 3. Results and discussion

#### 3.1. Effects of shape

The seminal work of (Durham *et al.* 2009) demonstrated that the critical shear  $S_C$ , at which gyrotactic microswimmers accumulate, can be predicted as  $1/\tau$  based on the torque balance equation. The critical shear,  $S_C = 1/\tau$ , arises from the torque balance between hydrodynamic and gravitational torques acting on a gyrotactic microswimmer. At steady state, (2.10) simplifies to  $\partial u/\partial z = \sin \phi/\tau$ . Considering that the settling speed is much smaller than the swimming speed, the steady polar angle  $\phi$  is close to  $\pi/2$ , meaning  $\sin \phi$  is close to 1. Thus, the critical shear is approximately  $1/\tau$ . When we consider ellipsoid microswimmers of the same  $d_s$ , the larger aspect ratios  $\lambda$  alter the gyrotactic time scale  $\tau$ , leading to a smaller  $S_C$  (2.5). Additional observation can be done for figure 4, when simulations reach a steady state. Here, steady state refers to a statistically stationary condition where ensemble-averaged quantities, such as mean depth  $z$  and polar angle  $\phi$ , stabilise without consistent directional changes over a sufficiently long time window, even though individual trajectories may oscillate due to time-dependent shear or rotational diffusivity. As the aspect ratio of the microswimmer increases, the microswimmers are observed to accumulate at a smaller critical shear level.

In addition, we observe some nuanced behaviour of the accumulation depth in figure 5. The accumulation depth is typically slightly higher than the predicted critical shear depth. In figure 5(a), we see that the peaks of the probability density functions (PDFs) of the accumulation depths are higher than the critical shear depths. A similar effect is also seen in figure 5(b). The reason behind this is closely related to the mechanism of the thin-layer generation. Below the critical shear depth, the gravitational torque dominates,



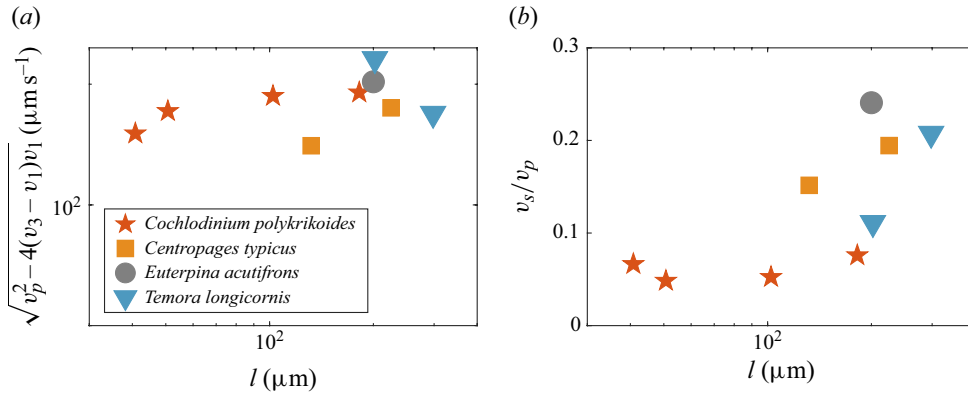


Figure 6. (a) Plot of  $\sqrt{v_p^2 - 4(v_3 - v_1)v_1}$  against the body lengths of four common types of gyrotactic microswimmers (Titelman 2001; Titelman & Kjørboe 2003; Carlotti, Bonnet & Halsband-Lenk 2007; Sohn *et al.* 2011). (b) The ratio of swimming speed and settling speed as a function of body length.

and microswimmers tend to move upward due to intrinsic mobility. Above critical shear hydrodynamic torque dominates, and microswimmers rotate continuously. As a result of this rotation, the intrinsic mobility contributes negligibly to the net vertical displacement, and microswimmers sink due to gravitational settling. The microswimmers' settling velocities are much smaller than their intrinsic mobility, as shown in figure 6. Hence, the time for microswimmers to stay above the critical shear is longer than the time below in the predicted critical shear. Consequently, the thin layer appeared to be a little above the critical shear depth. This phenomenon was also observed in the experiments of (Durham *et al.* 2009).

In addition, the larger aspect ratios will also lead to thicker layers. This is evidenced by the more scattered trajectories while the aspect ratio  $\lambda$  increases (figure 4). In figure 5(a), we observe that the PDF is more widespread as the aspect ratio increases. In the inset, we plot the PDFs' standard deviation as the characterisation of the thin-layer thickness, and we observe a monotonic increase in layer thickness with an increase in the aspect ratio.

The thicker layer for microswimmers with larger aspect ratios can be explained by carefully observing (2.10). Particles rotate slower with increasing  $\lambda$  due to a larger  $\lambda^2 + 1$  in the denominator of angular velocity. In addition, larger aspect ratio microswimmers tend to accumulate at the depth with smaller shear, leading to a further decrease in the rotation rate. During the thin-layer accumulation, the microswimmers usually continuously rotate once their position is higher than the critical shear such that the microswimmer's intrinsic mobility is rotated in all possible directions in the  $x$ - $z$  plane. Over one rotation period in the  $x$ - $z$  plane, the intrinsic mobility of the swimmer causes displacement in all directions, resulting in a net displacement in the  $z$ -direction that is almost zero. The net-zero vertical displacement notwithstanding, the trajectories in  $t$ - $z$  space will be a sinuous line. The radius of curvature of the trajectory increases as the rotation rate decreases. When the microswimmer's aspect ratio increases, the rotation becomes slower, and the radius of curvature increases, causing thicker thin-layer accumulation.

### 3.2. The time scale of thin-layer accumulation

In addition to the gyrotactic time scale, there is also an important time scale: the time scale for microswimmers to accumulate at the thin layer ( $t_d$ ), which is crucial for understanding how microswimmers accumulate in time-dependent flows where critical shear depth

is changing. We rewrite (2.10) as (3.1) and focus on the  $z$  component of (2.12) to obtain (3.2). These two differential equations describe the variation of polar angle  $\phi$  and vertical position  $z$  for microswimmers, while noise is neglected. Here, we perform a linear stability analysis on the following dynamic system:

$$\frac{d\phi}{dt} = \frac{1}{1+\lambda^2} \left( \frac{\partial u_x}{\partial z} - \frac{p_x}{\tau} \right), \quad (3.1)$$

$$\frac{dz}{dt} = v_p p_z - \left[ v_1 + (v_3 - v_1) p_z^2 \right], \quad (3.2)$$

where  $u_x$  is the projection of flow speed in the  $x$  direction,  $p_x$  is the projection of the swimming direction vector  $\mathbf{p}$  onto the  $x$ -axis and  $p_z$  is the projection of  $\mathbf{p}$  onto the  $z$ -axis. The fixed point is obtained as

$$\cos \phi^* = \frac{v_p - \sqrt{v_p^2 - 4(v_3 - v_1)v_1}}{2(v_3 - v_1)}, \quad (3.3)$$

$$S(z^*) = \frac{\sqrt{1 - \cos^2 \phi^*}}{\tau}, \quad (3.4)$$

$$v_p \cos \phi^* = v_1 + (v_3 - v_1) \cos^2 \phi^* = v_s, \quad (3.5)$$

where  $z^*$  and  $\phi^*$  are steady-state solutions to the dynamical system and  $v_s$  is the vertical component of  $\mathbf{v}_{settle}$ . To ensure the existence of the fixed points, we compare the values of  $v_p^2$  and  $4(v_3 - v_1)v_1$  for a series of common gyrotactic swimmer species in figure 6(a). Typically, a microswimmer's intrinsic mobility is much larger than the settling velocity (Kamykowski, Reed & Kirkpatrick 1992), ensuring that fixed points always exist for microswimmers. To analyse the stability of the equilibrium points, the Jacobian is derived as follows:

$$J = \begin{bmatrix} -\frac{1}{1+\lambda^2} \frac{\cos \phi}{\tau} & \frac{1}{1+\lambda^2} S'(z) \\ -v_p \sin \phi + 2 \cos \phi \sin \phi (v_3 - v_1) & 0 \end{bmatrix}, \quad (3.6)$$

where  $S'(z) = \partial^2 u / \partial z^2$  is the shear changing rate. Eigenvalues of the Jacobian are obtained as follows:

$$\sigma_{1,2} = \frac{1}{2} \left[ -\frac{1}{1+\lambda^2} \frac{\cos \phi^*}{\tau} \pm \sqrt{\left( \frac{1}{1+\lambda^2} \frac{\cos \phi^*}{\tau} \right)^2 - \frac{4S'(z^*)}{1+\lambda^2} [v_s \sin \phi^* - (v_3 - v_1) 2 \sin \phi^* \cos \phi^*]} \right]. \quad (3.7)$$

Let  $M = (\cos \phi^* / ((1 + \lambda^2)\tau))^2$  and  $N = 4S'(z^*) / (1 + \lambda^2) [v_p \sin \phi^* - (v_3 - v_1) 2 \sin \phi^* \cos \phi^*]$ , the eigenvalues can be simplified as

$$\sigma_{1,2} = \frac{-\sqrt{M} \pm \sqrt{M - N}}{2}. \quad (3.8)$$

We identify two regimes of eigenvalues: regime I with  $M < N$  and regime II with  $M \geq N$ . In regime I, the eigenvalues have a negative real part and an imaginary part, which indicates the equilibrium points are stable. On the other hand, if  $M \geq N$ , the

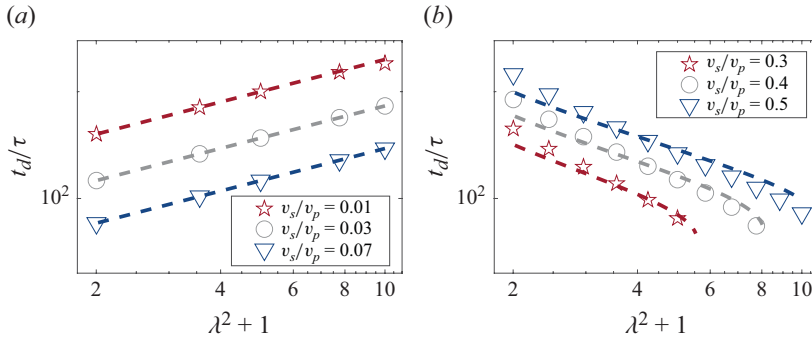


Figure 7. Plots of thin-layer accumulation time scale ( $t_d$ ) normalised by particle's gyrotactic time scale ( $\tau$ ) versus  $\lambda^2 + 1$  with a series of speed ratios  $v_s/v_p$ , where dashed lines represent theoretical predictions, and markers show numerical results. (a) Plots in regime I and (b) plots in regime II.

eigenvalues are real numbers, and  $\sqrt{M}$  is always greater than  $\sqrt{M - N}$ , indicating that the equilibrium points are still stable. The existence of a stable fixed point for all cases indicates that thin-layer formation is possible for all motile microswimmers.

We estimate the time scale  $t_d$  for microswimmers to accumulate at the thin layer during the initial transient stage as  $t_d = 2/\sqrt{M}$  when  $M < N$  (regime I) and  $t_d = 2/(\sqrt{M} - \sqrt{M - N})$  when  $M \geq N$  (regime II). If  $M < N$ ,  $t_d$  in regime I can be rewritten as follows by substituting the definition of  $A$  and  $\cos \phi^* = v_s/v_p$  into the expression:

$$\frac{t_d}{\tau} = \frac{2(1 + \lambda^2)}{v_s/v_p}. \quad (3.9)$$

The time scale ratio  $t_d/\tau$  is directly proportional to  $1 + \lambda^2$ , and inversely proportional to the speed ratio  $v_s/v_p$ . In the simulation results, we measure the decaying time scale  $t_d$  by fitting the  $z-t$  curve with an exponential function. Figure 7 compares the numerical estimation with theoretical results of decaying time scales in two regimes with a series of aspect ratios.

In regime I, the simulation results match the theoretical predictions perfectly, where  $t_d/\tau$  monotonically increases with  $\lambda^2 + 1$  according to (3.9). In regime II,  $t_d/\tau$  decreases as  $\lambda^2 + 1$  increases according to our theoretical prediction. However, the numerical results in regime II (figure 7b) show a larger error compared with regime I (figure 7a) due to the influence of a secondary eigenvalue in (3.8). In regime II, the two real eigenvalues correspond to different decaying time scales, and our prediction uses the larger time scale, corresponding to the eigenvalue with a smaller magnitude. The secondary eigenvalues, associated with a faster decay, can alter the numerical results, leading to the observed discrepancy. As  $\lambda$  increases, the term  $M$  decreases faster than the term  $N$  until a point where  $M = N$ , initiating the transition from regime II to regime I.

### 3.3. Effects of time-dependent background flow

In this section, we will answer the following question: Will a fast-changing flow disrupt the accumulation of gyrotactic microswimmers? This is an important, unanswered question because the flow is time varying in most natural environments, and understanding how the time variation of the background flow impacts microswimmers will enable us to better understand the widely observed thin-layer formation in natural water bodies.

A perturbation term  $\epsilon \sin \omega t$  is added to the original fixed shear profile (figure 2b) and the shear rate becomes  $\partial u/\partial z = 3z - 0.3 + \epsilon \sin \omega t$ , where  $\epsilon = 0.1 \text{ s}^{-1}$ . With this

perturbation term, the vertical position of the critical shear varies as a sine wave with time. The  $\omega$  values used in our simulation are  $5 \times 10^{-2}$ ,  $5 \times 10^{-3}$ ,  $5 \times 10^{-4}$  and  $5 \times 10^{-5} \text{ s}^{-1}$ . The reason why we chose this kind of flow is that the critical shear also oscillates sinusoidally in linear gravity waves with the deep water limit and small wave amplitude, and the linear gravity wave can be the source of time dependence in natural water bodies. Here, we neglect the vertical variation of the oscillations from linear gravity waves. Although more general time-dependent perturbations warrant exploration, their analysis lies beyond the scope of this work and deserves future study. The parameters of microswimmers are the same as those described in § 2.2. Considering the possible influence of initial conditions, we release 100 particles at five heights,  $z_0 = 0.05$ ,  $z_0 = 0.1$ ,  $z_0 = 0.15$ ,  $z_0 = 0.2$  and  $z_0 = 0.25 \text{ m}$ . These heights cover the range of heights where the critical shear exists. The initial orientations of the particles are randomised with a uniform distribution, and the time step is set to 0.1 s. This time step is found to be sufficient to simulate the swimmer dynamics accurately given the smaller translational and rotational movement of the microswimmers. In order to distinguish different regimes clearly, we removed the rotational diffusivity in the simulation because it would cause the thin layer to become thicker. Nevertheless, the regimes discussed here still persist when a sufficiently small rotational diffusivity is added. As the rotational diffusivity increases, the distinction between different thin-layer regimes gradually disappears. In the following, we only present the results for microswimmers with  $\lambda = 2$ , but the result also holds for other body shapes.

To quantify the time period of background flow  $T = 2\pi/\omega$  relative to  $t_d$ , we define a dimensionless number  $R = t_d/T$ . A typical guess would be that, if  $t_d < T$ , the microswimmer would accumulate, and the accumulation would disappear if  $t_d > T$ . Surprisingly, the thin-layer accumulation will occur regardless of the relative difference between  $t_d$  and  $T$ , and we identified three distinct regimes with distinct behaviours.

Before we look into the details of the three distinct behaviours, we define another time scale ( $t_r$ ) that describes the mean time required for a swimmer to rotate  $2\pi$  due to a hydrodynamic torque when hydrodynamic torque dominates the gravitational torque. From (3.1), we can express the rotation time scale

$$t_r = \int_0^{2\pi} \frac{1 + \lambda^2}{\frac{\partial u_x}{\partial z} - \frac{\sin \theta}{\tau}} d\theta. \quad (3.10)$$

When hydrodynamic torque is dominant, we have  $\partial u_x/\partial z > 1/\tau$ . However, we are specifically interested in cases where the microswimmer is not too far from the critical shear level, ensuring that  $t_r$  remains meaningful for understanding thin-layer formation. Consequently, we cannot ignore the term  $\sin \theta/\tau$ . Assuming  $\partial u_x/\partial z$  to be constant, we have

$$t_r = \frac{2\pi(1 + \lambda^2)}{\sqrt{\left(\frac{\partial u_x}{\partial z}\right)^2 - \frac{1}{\tau^2}}}. \quad (3.11)$$

However, for realistic  $t_r$  estimation with time-dependent shear for our specific case, we numerically calculate this time scale with time-varying shear. We calculate  $t_r$  by placing microswimmers at 0.25 m in our flow, which is close to the time-varying shear for microswimmers of different aspect ratios, where the hydrodynamic torque is always dominant. Choosing the depth to calculate  $t_r$  seems arbitrary, but our results hold for a variety of depths with the following two criteria: (i) the depth should always have

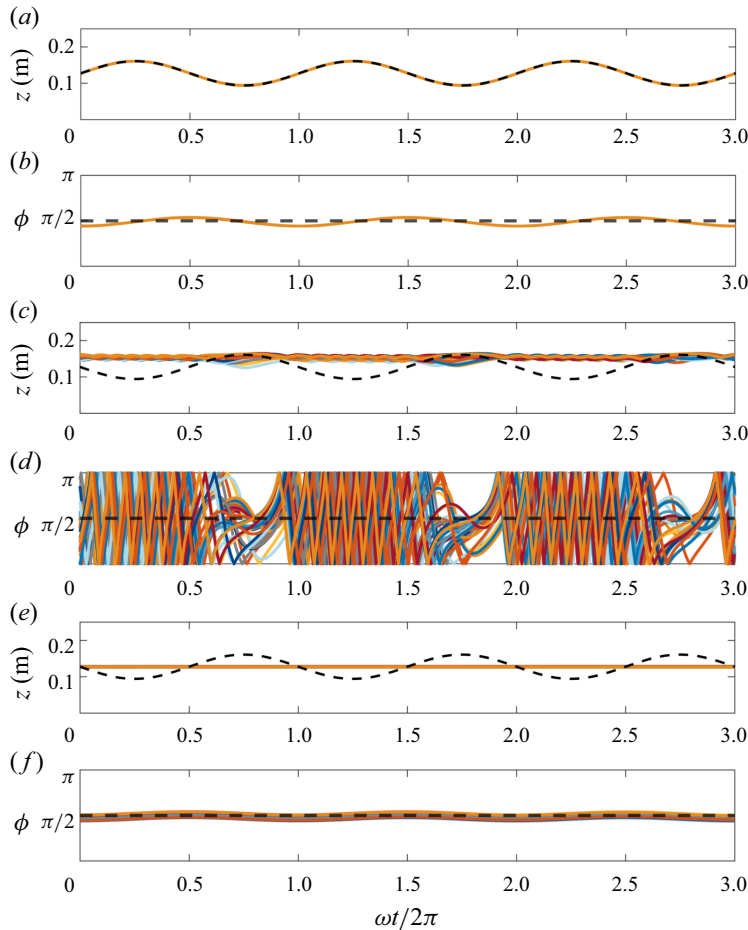


Figure 8. Time evolutions of height and polar angle of a group of particles ( $\lambda=2$ ) against normalised time over 3 periods after the simulation reach a steady state with (a) and (b)  $\omega = 5 \times 10^{-5}$  (regime A), (c) and (d)  $\omega = 5 \times 10^{-4}$  (regime B), (e) and (f)  $\omega = 5 \times 10^{-2}$  (regime C). Dashed lines in (a), (c) and (e) show the time variation of the height of critical shear. Dashed lines in (b), (d) and (f) indicate horizontal polar angle. For all cases, microswimmers are initially released at  $z_0 = 0.05$ ,  $z_0 = 0.1$ ,  $z_0 = 0.15$ ,  $z_0 = 0.2$  and  $z_0 = 0.25$  m with random orientations.

hydrodynamic torque dominance and (ii) the depth should be close to the critical shear depths, such that the magnitude of the shear is on the similar order of magnitude of critical shear. The numerical estimation of  $t_r$  is reasonably close to the one estimated by (3.11). With  $t_r$ , we can define another non-dimensional number:  $V = t_r/T$ . Later, we will demonstrate that  $V$  and  $R$  are linearly related, and  $V$  is a better parameter to separate the three regimes. With the time scales derived, we will present three representative cases for three regimes.

Regime A occurs when  $V < 10^{-2}$ . Our case A has  $R = 0.25$  and  $V = 0.004$ . In figure 8(a), we observe that the swimmers' depths closely follow the depth of the critical shear. This is intuitive because background flow varies so slowly that its time scale is several times larger than the time scale required to accumulate the thin layer ( $t_d$ ), and the background flow time scale is three orders of magnitude slower than the rotation time scale when hydrodynamic forces dominate ( $t_r$ ). In this case, microswimmer depth closely follows the depth of critical shear, and the polar angle ( $\phi$ ) slowly oscillates around the

$\pi/2$  with a small amplitude (figure 8*b*). The slowly oscillating  $\phi$  directs  $v_z$  up and down, allowing the swimmers to follow the critical shear depth. The  $z$ - $t$  and  $\phi$ - $t$  curves have the same frequency but exhibit a  $\pi/2$  phase shift.

Regime B occurs when  $V \in (10^{-2}, 10^{-1})$ . Our case B has  $R = 2.5$  and  $V = 0.04$ . In figure 8(*c*), we observe that the microswimmers accumulate at the highest elevation of the varying critical shear depth. The value  $R = 2.5$  indicates that microswimmers cannot closely follow the critical shear depth. At a steady state, when the critical shear depth goes down, the microswimmers are not able to follow it. Instead, microswimmers experience local shear that is larger than the critical shear because shear increases as a function of  $z$ . During this time, microswimmers rotate continuously due to the dominant hydrodynamic torque. As a consequence, microswimmers will sink due to gravity. Since  $V \ll 1$ , between the time gap ( $T$ ) when critical shear reaches the highest point, microswimmers will rotate  $N$  times with  $N \gg 1$ . This large number of rotations ( $N \gg 1$ ) minimises the intrinsic mobility's contribution to the net displacement in  $z$  during  $T$ . Since the settling velocity for the microswimmer is very small, the  $z$  displacement due to gravity is small during  $T$ . When the critical shear occurs above the swimmers' positions, gravitational torque dominates, directing the microswimmer to move upward. The microswimmers repeat this process over time. Nevertheless, the  $z$  displacement is small, so the microswimmers appear to be accumulated in a thin layer. In figure 8(*d*), the value of  $\phi$  oscillates between 0 and  $\pi$  when the critical shear depth is lower than the thin-layer depth, indicating that the microswimmer rotates due to the dominant hydrodynamic shear. As a consequence, this rotation results in small oscillations in  $z$  as a function of time when the critical shear depth is below the thin-layer depth. During the brief periods where the critical shear is higher than the microswimmers, the polar angle ( $\phi$ ) oscillation stops due to gravitational torque dominance and  $\phi$  approaches 0 due to the dominant gravitational torque.

Regime C occurs when  $V > 1$ . Our case C has  $R = 250$  and  $V = 4$ . In figure 8(*e*), we observe that the microswimmers accumulate at the mean location of the critical shear. A value of  $V > 1$  indicates that microswimmers will rotate only a fraction of  $2\pi$  during  $T$ . If a microswimmer is located above the mean elevation of the critical shear, hydrodynamic shear dominates for a larger fraction of the time (when viewed from the microswimmer's frame of reference). This dominance causes the microswimmer to rotate continuously while its settling velocity gradually reduces its elevation. Conversely, if a microswimmer is initially lower than the mean critical shear location, it will experience more dominant gravitational torque over time (i.e. the fraction of time the microswimmer experiences dominant gravitational torque is larger), which will direct it to a higher position. Only when the microswimmer is at the mean location of the critical shear will it experience half-time with dominant gravitational torque and half-time with dominant hydrodynamic torque. This is evidenced by the time evolution of the polar angle as shown in figure 8(*f*). The small amplitude of  $\phi$  is due to the short duration of  $T$  in this regime, where the microswimmer's orientation changes minimally under any applied torque.

Between regimes B and C, we observe a transitional regime where  $V \in (10^{-1}, 10^0)$ . In this case, a microswimmer will rotate  $N$  times during  $T$  if the microswimmer is in a hydrodynamic dominant shear and  $N \in (1, 10)$ . Nevertheless,  $N$  is not large enough, and the initial depths can play a role. Our simulations reveal that, depending on the initial  $z$  position, a microswimmer will reach different steady-state elevations (figure 9*d*).

To have a better understanding of regimes A, B and C, as well as the transitional regime, we plot the trajectories of microswimmers in a space spanned by  $z$  and  $\phi$ . Figure 9 shows the four regimes, and we only consider the time when the simulation reaches a steady state. The number of periods plotted in figure 9 (10 for regime A, 40 for regime B, 8000

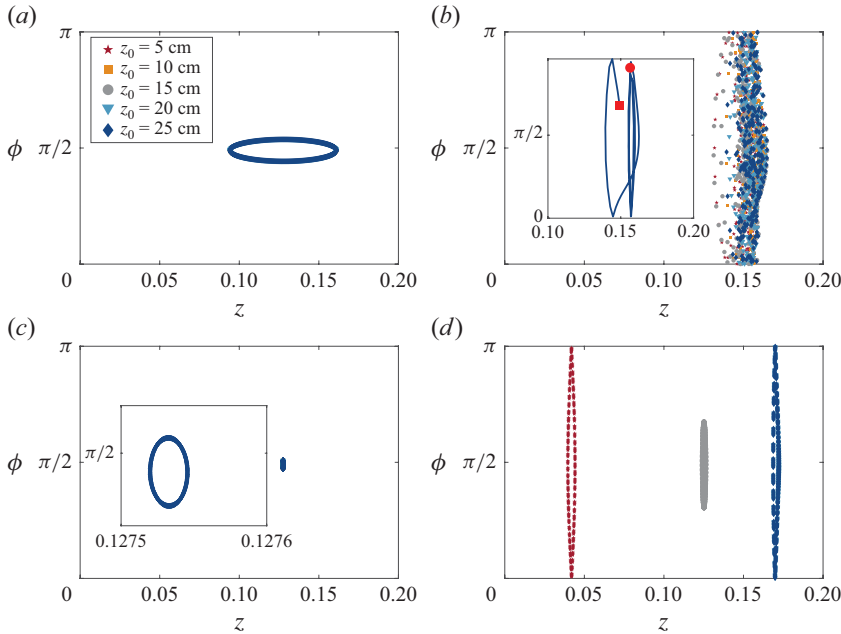


Figure 9. Microswimmer trajectories in  $\phi$ - $z$  space for (a) regime A, (b) regime B, (c) regime C and (d) transition regime after simulations reach steady state. The time windows are 10 periods for regime A, 40 periods for regime B, 8000 periods for regime C and 500 periods for the transitional regime. For each case, the trajectories of five particles are plotted, starting from different initial elevations ( $z_0 = 0.05$ ,  $z_0 = 0.1$ ,  $z_0 = 0.15$ ,  $z_0 = 0.2$  and  $z_0 = 0.25$  m). To clearly display the trajectories, one point is plotted every 25 s. The inset figure of (b) shows a segment of a microswimmer's trajectory after the simulation reaches a steady state, with the red rectangle indicating the starting point and the red circle marking the ending point. The inset in (c) provides a zoomed-in view of the trajectory.

for regime C and 500 for the transitional regime) was chosen to clearly depict the steady-state behaviour with a long enough total time (between  $5 \times 10^5$  and  $1 \times 10^6$  s). We see that the thin-layer accumulations for regimes A and C are associated with islands of stability. Even though regime B also has thin-layer accumulation behaviour, it does not show stable islands. As explained earlier, thin layers in regime B arise from alternating periods of continuous rotation due to hydrodynamic torque dominance and periods of gravitational torque dominance, rather than true stability. A closer examination of the trajectories in  $\phi$ - $z$  reveals that microswimmers spend more time at a higher position, which is exemplified by denser clouds of dots. At a higher position, hydrodynamic shear is dominant, which corresponds to the period when critical shear is between the peak position. During the hydrodynamic dominant period, settling velocity gradually sinks microswimmers. On the other hand, when microswimmers sink below the critical shear, gravitational torque dominates and directs them upward. From figure 6(b), we know that a microswimmer's swimming speed is significantly greater than its settling speed, causing microswimmers to spend less time at lower positions in the thin layer. This mechanism is similar to the behaviour observed in time-independent flow. In that case, the unsteadiness originated from the rotational diffusivity, while in regime B, the unsteadiness was due to flow time dependency. In the inset of figure 9(b), we illustrate the trajectory of one microswimmer in  $\phi$ - $z$  space. We clearly observe the continuous period of rotation linked to a slow decrease in  $z$ , and a quick decrease in  $\phi$  due to gravitational torque, which is accompanied by a relatively quicker increase in  $z$ . Interestingly, we observe three islands



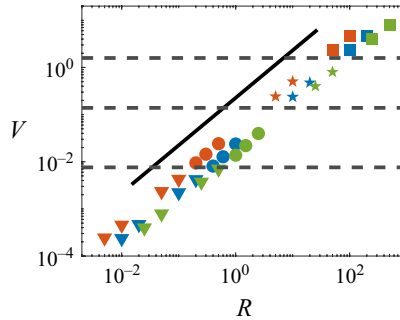


Figure 10. Phase diagram of multiple regimes in a time-varying background flow with non-dimensional numbers  $R$  and  $V$ . Triangles correspond to regime A; circles correspond to regime B; stars correspond to the transitional regime; squares correspond to regime C. Green symbols correspond to  $\lambda = 2$ ; blue symbols correspond to  $\lambda = 1.5$ ; red symbols correspond to  $\lambda = 1.001$ . The solid line represents a line with a slope of 1.

of stability in the transitional regime. But the period of the orbit is across a few flow periods ( $T$ ). In addition, the location for thin-layer formation is dependent on the initial elevation ( $z_0$ ). Across all regimes, where the flow–swimmer time scale ratio spans more than five orders of magnitude, microswimmers tend to accumulate in relatively thin layers. This explains why thin layers of planktonic life are widely observed in natural water bodies.

We summarise all three regimes and the transition regime in figure 10. It shows a clear linear relationship between  $V$  and  $R$ , indicating a linear relationship between  $t_d$  and  $t_r$ :  $t_d = ct_r + d$ , where  $c = 62.5$  and  $d \approx 0$ . This linear relationship simply means that the microswimmer, on average, tends to rotate  $c$  times before accumulation. The exact value of the constant  $c$  is not particularly important. However, the linear relationship between  $t_d$  and  $t_r$  shows that, the faster the microswimmer rotates, the quicker the microswimmers accumulate.

#### 4. Conclusion

We have examined the thin-layer formation dynamics of non-spherical phytoplankton (small motile particles) in time-dependent shear flow. From the balance between gravitational and hydrodynamic torques, we found that the equation for a swimmer's angular velocity consisted of an exponentially decaying term and a steady term. For microswimmers of sizes up to  $10^{-3}$  m and aspect ratios between 1 and 5, we showed that the exponential decay time scale is no greater than  $10^{-2}$  s, indicating that the system is highly damped. Thus, we can ignore this exponentially decaying term, and the angular speed of all gyrotactic microswimmers is determined by their shape, instantaneous orientation and local shear.

We showed that the higher aspect ratio microswimmers tend to accumulate at a smaller critical shear level. Our theoretical prediction of critical shear for non-spherical microswimmers agreed well with the simulation data. In the simulation, microswimmers tend to accumulate at a higher depth than predicted. This discrepancy arises from the speed asymmetry between sinking and gyrotaxis above and below the predicted height. Additionally, we observed that the microswimmer with higher aspect ratios would have a higher layer thickness due to a slower rotation rate.

Using linear stability analysis, we showed that stable fixed points exist for typical microswimmers in hydrodynamic shear. In addition, we derived a time scale ( $t_d$ ) for a

microswimmer to accumulate at critical shear and identified two regimes of the time scale. We validated the time scales using numerical simulation.

Finally, we studied the thin-layer accumulation dynamics with time-dependent flow, where the critical shear depth varies in a sinusoidal manner. As the time scale of the flow changes, we identified three distinct regimes and one transitional regime. When  $V < 10^{-2}$  (regime A), the flow time scale is much larger, and the microswimmer accumulation will closely follow the depth of the critical shear. Regime B occurs when  $V \in (10^{-2}, 10^{-1})$ . In this regime, microswimmers are not fast enough to closely follow the critical shear depth and instead accumulate at the highest elevation of the critical shear. Regime C exists when  $V > 1$ . The microswimmers tend to stay at the mean location of the swimmer. There is also a transitional regime with  $V \in (10^{-1}, 10^0)$ . We found that the microswimmer's behaviour is highly dependent on the initial conditions in this transitional regime. Despite this dependency, microswimmers eventually reach a steady-state elevation. Our research shows that a thin layer will form no matter the time scale of the background flow. This explains why thin layers of phytoplankton are ubiquitous in the natural water bodies where flow is time-dependent.

**Funding.** The work is supported by National Science Foundation CMMI-2143807 (L.F.) and CBET-2429374 (L.F.).

**Declaration of interests.** The authors report no conflict of interest.

**Author contributions** L.F. conceived the original idea and supervised the project. Z.L. conducted the simulation and analysis. Both authors contributed to the writing.

## REFERENCES

- ALLDREDGE, A.L., COWLES, T.J., MACINTYRE S, S., RINES, J.E.B., DONAGHAY, P.L., GREENLAW, C.F., HOLLIDAY, D.V., DEKSHENIEKS, M.M., SULLIVAN, J.M. & ZANEVELD, J.R.V. 2002 Occurrence and mechanisms of formation of a dramatic thin layer of marine snow in a shallow Pacific fjord. *Mar. Ecol. Prog. Ser.* **233**, 1–12.
- ARMI, L. 1978 Some evidence for boundary mixing in the deep ocean. *J. Geophys. Res.: Oceans* **83** (C4), 1971–1979.
- BEARON, R.N. & DURHAM, W.M. 2023 Elongation enhances migration through hydrodynamic shear. *Phys. Rev. Fluids* **8** (3), 033101.
- BERMAN, S.A., FERGUSON, K.S., BIZZAK, N., SOLOMON, T.H. & MITCHELL, K.A. 2022 Noise-induced aggregation of swimmers in the Kolmogorov flow. *Frontiers Phys.* **9**, 816663.
- BORGNO, M., BOFFETTA, G., CENCINI, M., DE LILLO, F. & GUSTAVSSON, K. 2022 Alignment of elongated swimmers in a laminar and turbulent Kolmogorov flow. *Phys. Rev. Fluids* **7** (7), 074603.
- BORGNO, M., BOFFETTA, G., DE LILLO, F. & CENCINI, M. 2018 Gyrotactic swimmers in turbulence: shape effects and role of the large-scale flow. *J. Fluid Mech.* **856**, R1.
- BORGNO, M., GUSTAVSSON, K., DE LILLO, F., BOFFETTA, G., CENCINI, M. & MEHLIG, B. 2019 Alignment of nonspherical active particles in chaotic flows. *Phys. Rev. Lett.* **123** (13), 138003.
- CARLOTTI, F., BONNET, D. & HALSBAND-LENK, C. 2007 Development and growth rates of *Centropages typicus*. *Prog. Oceanogr.* **72** (2–3), 164–194.
- DEKSHENIEKS, M.M., DONAGHAY, P.L., SULLIVAN, J.M., RINES, J.E.B., OSBORN, T.R. & TWARDOWSKI, M.S. 2001 Temporal and spatial occurrence of thin phytoplankton layers in relation to physical processes. *Mar. Ecol. Prog. Ser.* **223**, 61–71.
- DRESCHER, K., LEPTOS, K.C., TUVAL, I., ISHIKAWA, T., PEDLEY, T.J. & GOLDSTEIN, R.E. 2009 Dancing volvox: hydrodynamic bound states of swimming algae. *Phys. Rev. Lett.* **102** (16), 168101.
- DURHAM, W.M., CLIMENT, E., BARRY, M., DE LILLO, F., BOFFETTA, G., CENCINI, M. & STOCKER, R. 2013 Turbulence drives microscale patches of motile phytoplankton. *Nat. Commun.* **4** (1), 2148.
- DURHAM, W.M., CLIMENT, E. & STOCKER, R. 2011 Gyrotaxis in a steady vortical flow. *Phys. Rev. Lett.* **106** (23), 238102.
- DURHAM, W.M., KESSLER, J.O. & STOCKER, R. 2009 Disruption of vertical motility by shear triggers formation of thin phytoplankton layers. *Science* **323** (5917), 1067–1070.

- DURHAM, W.M. & STOCKER, R. 2012 Thin phytoplankton layers: characteristics, mechanisms, and consequences. *Annu. Rev. Mar. Sci.* **4** (1), 177–207.
- FALKINHOFF, F., OBLIGADO, M., BOURGOIN, M. & MININNI, P.D. 2020 Preferential concentration of free-falling heavy particles in turbulence. *Phys. Rev. Lett.* **125** (6), 064504.
- FRANKS, P.J.S. 1995 Thin layers of phytoplankton: a model of formation by near-inertial wave shear. *Deep Sea Res. Part I: Oceanogr. Res. Papers* **42** (1), 75–91.
- GUSTAVSSON, K., BERGLUND, F., JONSSON, P.R. & MEHLIG, B. 2016 Preferential sampling and small-scale clustering of gyrotactic microswimmers in turbulence. *Phys. Rev. Lett.* **116** (10), 108104.
- HILL, N.A. & HÄDER, D.-P. 1997 A biased random walk model for the trajectories of swimming micro-organisms. *J. Theor. Biol.* **186** (4), 503–526.
- JEFFERY, G.B. 1922 The motion of ellipsoidal particles immersed in a viscous fluid. *Proc. R. Soc. Lond. A* **102** (715), 161–179.
- KAMYKOWSKI, D., REED, R.E. & KIRKPATRICK, G.J. 1992 Comparison of sinking velocity, swimming velocity, rotation and path characteristics among six marine dinoflagellate species. *Mar. Biol.* **113** (2), 319–328.
- KASAI, A., KURIKAWA, Y., UENO, M., ROBERT, D. & YAMASHITA, Y. 2010 Salt-wedge intrusion of seawater and its implication for phytoplankton dynamics in the Yura Estuary, Japan. *Estuarine Coast. Shelf Sci.* **86** (3), 408–414.
- KESSLER, J.O. 1985 Hydrodynamic focusing of motile algal cells. *Nature* **313** (5999), 218–220.
- KHURANA, N., BLAWZDZIEWICZ, J. & OUELLETTE, N.T. 2011 Reduced transport of swimming particles in chaotic flow due to hydrodynamic trapping. *Phys. Rev. Lett.* **106** (19), 198104.
- LOVECCHIO, S., CLIMENT, E., STOCKER, R. & DURHAM, W.M. 2019 Chain formation can enhance the vertical migration of phytoplankton through turbulence. *Sci. Adv.* **5** (10), eaaw7879.
- MOLINE, M.A., BENOIT-BIRD, K.J., ROBBINS, I.C., SCHROTH-MILLER, M., WALUK, C.M. & ZELENKE, B. 2010 Integrated measurements of acoustical and optical thin layers II: horizontal length scales. *Cont. Shelf Res.* **30** (1), 29–38.
- MONCHAUX, R., BOURGOIN, M. & CARTELLIER, A. 2012 Analyzing preferential concentration and clustering of inertial particles in turbulence. *Intl J. Multiphase Flow* **40**, 1–18.
- OBLIGADO, M., TEITELBAUM, T., CARTELLIER, A., MININNI, P. & BOURGOIN, M. 2014 Preferential concentration of heavy particles in turbulence. *J. Turbul.* **15** (5), 293–310.
- OSBORN, T. 1998 Finestructure, microstructure, and thin layers. *Oceanography* **11** (1), 36–43.
- PHILLIPS, O.M., SHYU, J.-H. & SALMUN, H. 1986 An experiment on boundary mixing: mean circulation and transport rates. *J. Fluid Mech.* **173**, 473–499.
- PUJARA, N., KOEHL, M.A.R. & VARIANO, E.A. 2018 Rotations and accumulation of ellipsoidal microswimmers in isotropic turbulence. *J. Fluid Mech.* **838**, 356–368.
- QIU, J., MARCHIOLI, C. & ZHAO, L. 2022 A review on gyrotactic swimmers in turbulent flows. *Acta Mechanica Sinica* **38** (8), 722323.
- RAY, B. & COLLINS, L.R. 2011 Preferential concentration and relative velocity statistics of inertial particles in Navier–Stokes turbulence with and without filtering. *J. Fluid Mech.* **680**, 488–510.
- RUSCONI, R., GUASTO, J.S. & STOCKER, R. 2014 Bacterial transport suppressed by fluid shear. *Nat. Phys.* **10** (3), 212–217.
- RYAN, J.P., MCMANUS, M.A., PADUAN, J.D. & CHAVEZ, F.P. 2008 Phytoplankton thin layers caused by shear in frontal zones of a coastal upwelling system. *Mar. Ecol. Prog. Ser.* **354**, 21–34.
- SANTAMARIA, F., DE LILLO, F., CENCINI, M. & BOFFETTA G. 2014 Gyrotactic trapping in laminar and turbulent Kolmogorov flow. *Phys. Fluids* **26** (11), 111901.
- SEURONT, L. & STRUTTON, P.G. 2003 Planktonic layers: physical and biological interactions on the small scale. In *Handbook of Scaling Methods in Aquatic Ecology*, pp. 51–70. CRC Press.
- SI, X. & FANG, L. 2021 Preferential alignment and heterogeneous distribution of active non-spherical swimmers near Lagrangian coherent structures. *Phys. Fluids* **33** (7), 052109.
- SI, X. & FANG, L. 2022 Preferential transport of swimmers in heterogeneous two-dimensional turbulent flow. *Phys. Rev. Fluids* **7** (9), 094501.
- SOHN, M.H., SEO, K.W., CHOI, Y.S., LEE, S.J., KANG, Y.S. & KANG, Y.S. 2011 Determination of the swimming trajectory and speed of chain-forming dinoflagellate *Cochlodinium polykrikoides* with digital holographic particle tracking velocimetry. *Mar. Biol.* **158** (3), 561–570.
- SQUIRES, K.D. & EATON, J.K. 1991 Preferential concentration of particles by turbulence. *Phys. Fluids A: Fluid Dyn.* **3** (5), 1169–1178.
- STOCKER, R. 2012 Marine microbes see a sea of gradients. *Science* **338** (6107), 628–633.
- SULLIVAN, J.M., DONAGHAY, P.L. & RINES, J.E.B. 2010 Coastal thin layer dynamics: consequences to biology and optics. *Cont. Shelf Res.* **30** (1), 50–65.

- TITELMAN, J. 2001 Swimming and escape behavior of copepod nauplii: implications for predator–prey interactions among copepods. *Mar. Ecol. Prog. Ser.* **213**, 203–213.
- TITELMAN, J. & KJØRBOE, T. 2003 Motility of copepod nauplii and implications for food encounter. *Mar. Ecol. Prog. Ser.* **247**, 123–135.
- TORNEY, C. & NEUFELD, Z. 2007 Transport and aggregation of self-propelled particles in fluid flows. *Phys. Rev. Lett.* **99** (7), 078101.
- WHEELER, J.D., SECCHI, E., RUSCONI, R. & STOCKER, R. 2019 Not just going with the flow: the effects of fluid flow on bacteria and plankton. *Annu. Rev. Cell Dev. Biol.* **35** (1), 213–237.
- YAZDI, S. & ARDEKANI, A.M. 2012 Bacterial aggregation and biofilm formation in a vortical flow. *Biomicrofluidics* **6** (4), 044114.
- ZHAN, C., SARDINA, G., LUSHI, E. & BRANDT, L. 2014 Accumulation of motile elongated micro-organisms in turbulence. *J. Fluid Mech.* **739**, 22–36.